A regional nuclear conflict would compromise global food security

Jonas Jägermeyr[a,b,c,1], Alan Robock[d], Joshua Elliott[a], Christoph Müller[c], Lili Xia[d], Nikolay Khabarov[e], Christian Folberth[e], Erwin Schmid[f], Wenfeng Liu[g,h], Florian Zabel[i], Sam S. Rabin[j], Michael J. Puma[b,k], Alison Heslin[b,k], James Franke[l], Ian Foster[a,m], Senthold Asseng[n], Charles G. Bardeen[o,p], Owen B. Toon[p], and Cynthia Rosenzweig[b,k]

[a]Department of Computer Science, University of Chicago, Chicago, IL 60637; [b]Goddard Institute for Space Studies, National Aeronautics and Space Administration, New York, NY 10025; [c]Climate Resilience, Potsdam Institute for Climate Impact Research, Member of the Leibniz Association, 14473 Potsdam, Germany; [d]Department of Environmental Sciences, Rutgers University, New Brunswick, NJ 08901; [e]Ecosystem Services and Management Program, International Institute for Applied Systems Analysis, 2361 Laxenburg, Austria; [f]Institute for Sustainable Economic Development, University of Natural Resources and Life Sciences, 1180 Vienna, Austria; [g]Laboratoire des Sciences du Climat et de l'Environnement, Université Paris-Saclay, 91191 Gif-sur-Yvette, France; [h]Department Systems Analysis, Integrated Assessment and Modeling, Swiss Federal Institute of Aquatic Science and Technology, 8600 Duebendorf, Switzerland; [i]Department of Geography, Ludwig-Maximilians-Universität München, 80333 Munich, Germany; [j]Institute of Meteorology and Climate Research, Atmospheric Environmental Research, Karlsruhe Institute of Technology, 82467 Garmisch-Partenkirchen, Germany; [k]Center for Climate Systems Research, Columbia University, New York, NY 10025; [l]Department of the Geophysical Sciences, University of Chicago, Chicago, IL 60637; [m]Data Science and Learning Division, Argonne National Laboratory, Lemont, IL 60439; [n]Agricultural & Biological Engineering Department, University of Florida, Gainesville, FL 32611; [o]Atmospheric Chemistry Observations and Modeling Laboratory, National Center for Atmospheric Research, Boulder, CO 80305; and [p]Department of Atmospheric and Oceanic Sciences, Laboratory for Atmospheric and Space Physics, University of Colorado, Boulder, CO 80303

A limited nuclear war between India and Pakistan could ignite fires large enough to emit more than 5 Tg of soot into the stratosphere. Climate model simulations have shown severe resulting climate perturbations with declines in global mean temperature by 1.8 °C and precipitation by 8%, for at least 5 y. Here we evaluate impacts for the global food system. Six harmonized state-of-the-art crop models show that global caloric production from maize, wheat, rice, and soybean falls by 13 (±1)%, 11 (±8)%, 3 (±5)%, and 17 (±2)% over 5 y. Total single-year losses of 12 (±4)% quadruple the largest observed historical anomaly and exceed impacts caused by historic droughts and volcanic eruptions. Colder temperatures drive losses more than changes in precipitation and solar radiation, leading to strongest impacts in temperate regions poleward of 30°N, including the United States, Europe, and China for 10 to 15 y. Integrated food trade network analyses show that domestic reserves and global trade can largely buffer the production anomaly in the first year. Persistent multiyear losses, however, would constrain domestic food availability and propagate to the Global South, especially to food-insecure countries. By year 5, maize and wheat availability would decrease by 13% globally and by more than 20% in 71 countries with a cumulative population of 1.3 billion people. In view of increasing instability in South Asia, this study shows that a regional conflict using <1% of the worldwide nuclear arsenal could have adverse consequences for global food security unmatched in modern history.

food system shock | multiple breadbasket failure | cold temperature yield response | India–Pakistan conflict | global gridded crop model intercomparison (GGCMI)

The continued existence of nuclear weapons implies a risk to life on Earth not just from the immediate effects of the war. Adverse indirect environmental and societal consequences of sudden climate change due to a potential nuclear conflict— especially for food production systems—were suggested during the Cold War era (1–5). If targeted on urban areas, even small air bursts by today's standards, such as the 15-kt weapon used on Hiroshima, could ignite large fires releasing large amounts of black carbon (soot). Once the smoke plume reaches the upper troposphere, soot would absorb solar radiation and self-loft into the stratosphere, where particles would spread globally within months (6). The smoke from a single fire would not produce detectable climate impacts, but cumulative emissions from many fires generating several teragrams of soot could substantially absorb sunlight in the stratosphere, so that less energy

reaches the Earth's surface, cooling it for about a decade (7, 8). Soot injection and resulting reductions in surface temperature and precipitation could be larger and longer lasting than after major volcanic eruptions such as Tambora (Indonesia) in 1815, which caused widespread crop failures, famine, and economic hardship (9).

Territorial disputes over the Kashmir region between India and Pakistan provide an increasingly high level of instability (10, 11), and escalatory retaliation could result in the use of nuclear weapons (12). This study highlights the indirect food system consequences of a possible, limited nuclear war based on a previously published India–Pakistan scenario, assuming 5 Tg of soot injection derived from a direct relationship between population density and target-specific fuel load (7, 13).

> ### Significance
>
> Impacts of global warming on agricultural productivity have been evaluated extensively. The implications of sudden cooling for global crop growth, however, are as yet little understood. While crop failures after historic volcanic eruptions are documented, a nuclear conflict can cause even more severe and longer-lasting climate anomalies. India and Pakistan are contributing to a de facto Asian arms race and the political instability in South Asia increasingly imposes a global threat. Based on comprehensive climate and crop model ensemble simulations, we provide critical quantitative information on how sudden cooling and perturbations of precipitation and solar radiation could disrupt food production and trade worldwide for about a decade—more than the impact from anthropogenic climate change by late century.

Climatic responses to large soot injections over South Asia have been studied systematically (8, 13–17). The impacts of such low-likelihood but severe events require careful investigation to inform the public and policy makers in view of nuclear proliferation and conflict. However, quantitative agricultural and economic impact assessments are lacking (5, 18). Simplified studies for single crops (5, 19) or individual locations in the United States or China (20–22) point to potentially large crop failures. But a critical knowledge gap exists regarding how such production disturbances unfold globally and potentially cause repercussions for the food trade system (23, 24). Here we present a comprehensive and internally consistent global-scale assessment framework, including state-of-the-art ensemble climate and crop model simulations of the production and trade responses of the major staple crops (maize, wheat, rice, and soybean) to a regional nuclear conflict, while explicitly quantifying the main sources of uncertainty.

We employ published climate simulations based on two versions of the Community Earth System Model (CESM) (25). To address uncertainties associated with smoke aerosols in the climate model, we complement simulations from 2014 (15) (climate forcing 1 [CF1]) with additional realizations based on the same 5-Tg scenario, but with an updated CESM and revised aerosol representation (13) (CF2). Both simulation sets provide three ensemble members starting from different initial conditions.

To convert the climate model forcing into bias-corrected inputs for high-resolution crop models, we use anomalies from climate model outputs to perturb an observational daily weather dataset (1981 to 2009) (26). This reduces climate model bias, preserves natural variability, and thus improves reliability of the crop modeling (27). Each postconflict year is simulated for 29 y of historical observations to identify interannual differences across years perturbed with identical forcing (*SI Appendix*, Fig. S1). Six well-established global mechanistic crop models (EPIC-BOKU, GEPIC, LPJmL, pDSSAT, PEPIC, and PROMET; see *SI Appendix*, Table S1 for details and full model names), as part of the global gridded crop model intercomparison (GGCMI) (28, 29), simulate impacts on crop production following a harmonized protocol; that is, harvested areas, growing periods, and fertilizer applications are externally prescribed through observational data. To avoid confounding effects from temporal trends, all inputs except weather are held constant in time (*Materials and Methods*).

Beyond direct domestic implications, large production anomalies can have cascading effects through the food trade system (23). To track the dynamics of multiyear production anomalies, we use a trade mass-balance network to evaluate changes in country-level food reserves and use (30). Observed data of maize and wheat production, reserves, and trade create network dependencies into which we introduce simulated annual production anomalies of both crops for 5 y after the conflict (we focus on maize and wheat to improve robustness; see *Materials and Methods*). Production shortfalls are compensated first by accessing reserves and drawing on food imports and then by reducing both domestic use and food exports, which propagate supply shocks to trade partners. India and Pakistan are excluded from the analysis by removing them from the trade network (to avoid arbitrary assumptions regarding the direct effects of the war; see below). Together, the simulated crop production anomalies and changes in trade-mediated food supply project overall impacts of a potential production shock on national food availability (*SI Appendix*, Fig. S1).

We address research questions that remain unresolved since the original studies of agricultural consequences of nuclear war (5): 1) Where, and to what degree, would global staple crop production be affected by a limited nuclear war? 2) How large are the main sources of uncertainty associated with the crop response? And 3) to what extent would trade dependencies

buffer and propagate production anomalies and impair food supply globally?

Climate Perturbations and Implications for Crop Production

Simulations of the 5-Tg soot case show attenuation of the incoming solar radiation, cooling of the surface, and weakening of the global hydrological cycle for at least a decade. An average of the first 5 y of the CF1 and CF2 climate anomalies shows declines in global mean surface air temperature by 1.8 °C, precipitation by 7.9%, and incoming shortwave and longwave solar radiation by 4.9% and 1.9%, respectively (Fig. 1; see *SI Appendix*, Fig. S2 for spatial pattern), producing the coldest average surface temperature in the last 1,000 y (9, 18, 31).

These climate perturbations reduce total global caloric production from maize, wheat, rice, and soybean by 10.8% (SD of crop models ±3.1%, other uncertainties addressed below) annually, averaged over the first 5 postconflict years (Fig. 2). Largest single-year losses are 12.4% (±4.0%) in year 4 after the conflict, which equals 4.8 times the historical SD (1981 to 2009) and exceeds by 2.7 times the largest observed anomaly in the record of the UN Food and Agricultural Organization (FAOSTAT) since 1961 (−4.6% in 2012, against the 1961 to 2017 average).

The crop impacts follow the characteristic timeline of the climate anomalies with a sharp decline and gradual recovery after 10 to 15 y (Fig. 3 and *SI Appendix*, Figs. S3–S6). While shortwave radiation anomalies peak within the first or second year, the temperature response is lagged by 3 to 4 y (Fig. 1) due to ocean thermal inertia and sea ice expansion (15). The CF2 simulations treat smoke as fractal particles and allow coagulation, which results in larger particles with a shorter lifetime and thus faster recovery compared to CF1 (13).

Maize—the linchpin in the global food system, accounting for about 35% of total global cereal production and trade (32) ("cereals" herein refer to all FAOSTAT cereal crops, plus
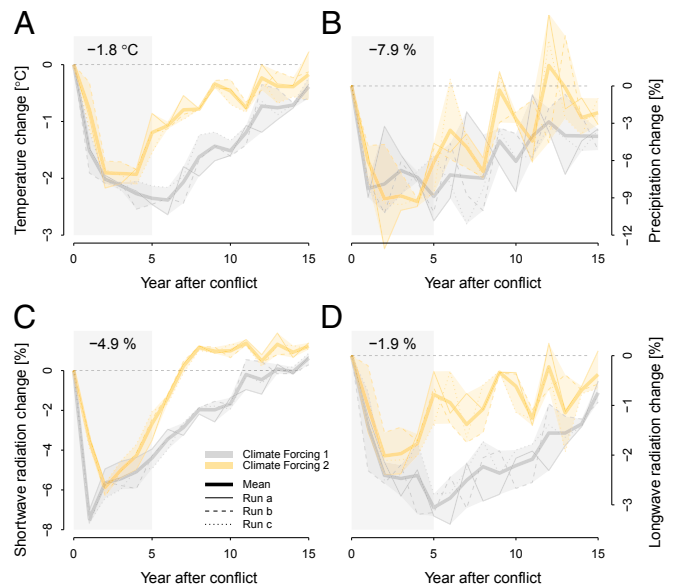
Fig. 1. Nuclear conflict-induced global climate perturbations. Changes in (*A*) 2-m air temperature (°C), (*B*) precipitation (%), and (*C*) surface incoming shortwave and (*D*) longwave solar radiation (%) are shown across 15 postconflict years for two climate simulation sets (climate forcing 1 and 2), with three ensemble members each (runs a–c). Changes are shown as absolute (temperature) and relative (all other variables) differences between control and perturbed global mean values, calculated over the global land area. The average year 1 to 5 change is highlighted on top of the shaded boxes.
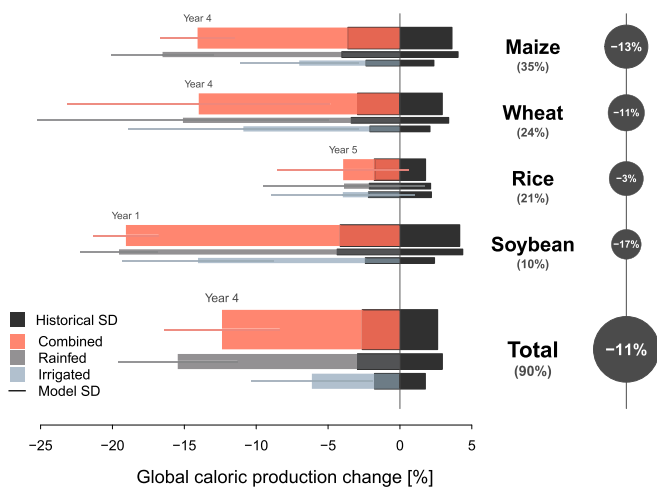
Fig. 2. Postconflict change of global staple crop production. Conflict-related impacts on global caloric production of maize, wheat, rice, soybean, and their total are shown for combined (red), rainfed (gray), and irrigated (blue) production. Changes are shown for the crop model ensemble mean (colored bars; the SD is indicated by horizontal lines) for the postconflict year with largest "combined" declines per crop (respective year is shown on top of the bar). All data are averaged across climate simulation sets. Black bars centered on the zero line illustrate the SD of unperturbed historical variability (1981 to 2009). Circled percentages highlight the 5-y postconflict average change. "Total" refers to the cumulated caloric production of the four crops, and percentage numbers in parentheses and the circle sizes indicate the respective fraction of current total global cereal production (including soybean). The bar width for total is increased to emphasize main results.

soybean)—shows production losses of 12.6% (±1.2%) globally, on average for 5 y after the conflict (Fig. 3). For the same time period, the United States and Canada (currently providing >40% of global maize production) would face 17.5% (±2.4%) production losses, China and East Asia (18% of global production) 6.3% (±1.2%), Europe (15% of global production) 16.7% (±5.5%), and Russia (1.8% of global production) 48.2% (±4.5%). The largest global single-year loss for maize is 14.1% (±2.6%) in postconflict year 4 (Fig. 2), which would be 60% more severe than in the historic 1988 drought year (−9% globally), the largest maize anomaly in the FAOSTAT record (*SI Appendix*, Fig. S7).

Production losses for wheat, the second most important global grain (24% of current cereal production), are 10.9% (±8.1%) globally for the 5-y average. While the peak impact (−14% ± 9.1% in year 4) is similar to that for maize, the crop model disagreement is substantially larger for wheat (ranging from −3 to −30%; Fig. 2). This is in part because wheat simulation responses differ for winter and spring varieties and in part because different vernalization requirements for winter wheat introduce spread in crop model results (33). Winter wheat shows larger 5-y average impacts (−13.3%; *SI Appendix*, Fig. S3) than spring wheat (−6.9%; *SI Appendix*, Fig. S4), because winter wheat experiences colder temperatures during its growing period that are more likely to cross critical thresholds.

Among all crops studied, rice (21% of cereal production) shows lowest overall losses; the 3.4% (±4.6%) loss in year 5 barely exceeds the historical SD (Fig. 2 and *SI Appendix*, Fig. S5). The crop model spread, however, is high (−9 to +4%). Soybean exhibits the largest global-scale impacts with 16.8% (±2.2%) production decline on average for 5 y, supported by robust model agreement (Fig. 2 and *SI Appendix*, Fig. S6). Yet, its contribution to total cereal production is only 10%. Together, the four crops account for 90% of current total global cereal production in caloric equivalents (32).

India and Pakistan are excluded from the analyses, not only to focus on climatic effects on agriculture in the rest of the world, but also because our analysis framework cannot account adequately for other direct effects of a war (radioactive fallout and negative effects on health, labor, and infrastructure). However, if both countries are included under the assumption that domestic staple crop production fails completely after the war, global caloric losses would increase from −11 to −19% (5-y average), mainly driven by production losses for wheat and rice (*SI Appendix*, Table S2).

Geographic Pattern, Uncertainty, and Attribution

Yield impacts follow a distinct geographic pattern, with declines >30% at latitudes beyond 30°N (Fig. 3), where surface temperature and shortwave radiation fall by >3 °C and >10%, respectively. Precipitation changes are spatially heterogeneous, with potential gains in Central America and the Mediterranean despite large reductions at higher latitudes (*SI Appendix*, Fig. S2). A latitudinal profile of crop yield losses suggests that all four crops follow largely similar response patterns, with main impacts poleward of 30°N and S, where climate impacts are greatest and where crop growth is increasingly temperature limited. However, the geographic distribution of current cropland extent differs substantially among crops (Fig. 4) and therefore leads to the differentiated overall production response. Rice, for instance, is predominantly grown between 30°N and S, which explains smaller overall impacts. The latitudinal profile of wheat yield declines, on the other hand, mainly coincides with the actual cropland extent. Moreover, rainfed systems generally experience more severe negative impacts (−14% global 5-y average) than irrigated systems (−6%) globally across all crops except rice (Fig. 2), in large part because irrigated systems are generally located at lower latitudes where temperature reductions are both smaller and less harmful to crops.

Overall, the developed world is shown to face the largest total crop losses, while lower-latitude tropical regions have less severe implications and even potential gains, although the latter is not supported by all crop models. Model agreement is greatest at higher latitudes, where differences between climate model realizations become more important than between crop models, while climate model disagreement remains small compared to the perturbation signal (Fig. 3).

Maize yield responses to single climate drivers individually perturbed one at a time reveal that temperature is the largest factor globally (−5.0%, 5-y average; Fig. 5 and *SI Appendix*, Fig. S8). Cooler temperatures affect high-latitude temperature-limited agriculture, primarily through failure to reach physiological maturity within a growing season and cold damage (*SI Appendix*, Fig. S9). The temperature response function of simulated maize yields appears to be linear between −1.5 and −4 °C local annual mean change (*SI Appendix*, Fig. S10). While precipitation (−2.5%), shortwave radiation (−3.7%), and longwave radiation (−0.9%) have smaller weights, this attribution shows that all factors are largely additive under this climate perturbation (−12.1% combined perturbation, 5-y average; Fig. 5). The crop models exhibit different response mechanisms to individual drivers, but they arrive at remarkably similar outcomes when collectively perturbed (*SI Appendix*, Fig. S8; more details in *SI Appendix*, Decomposition of Crop Model Responses).

We address three main sources of uncertainty in the integrated analysis: the climate model forcing from 5 Tg soot injection, the relative importance of the climate in the year in which the conflict occurs, and the crop model response itself. Decomposition of these uncertainty components reveals that they are roughly similar in overall contribution to simulated staple crop production under the nuclear conflict scenario (*SI Appendix*, Fig. S11). However, while the crop model response is the smallest source of uncertainty for maize and soy, it is the largest
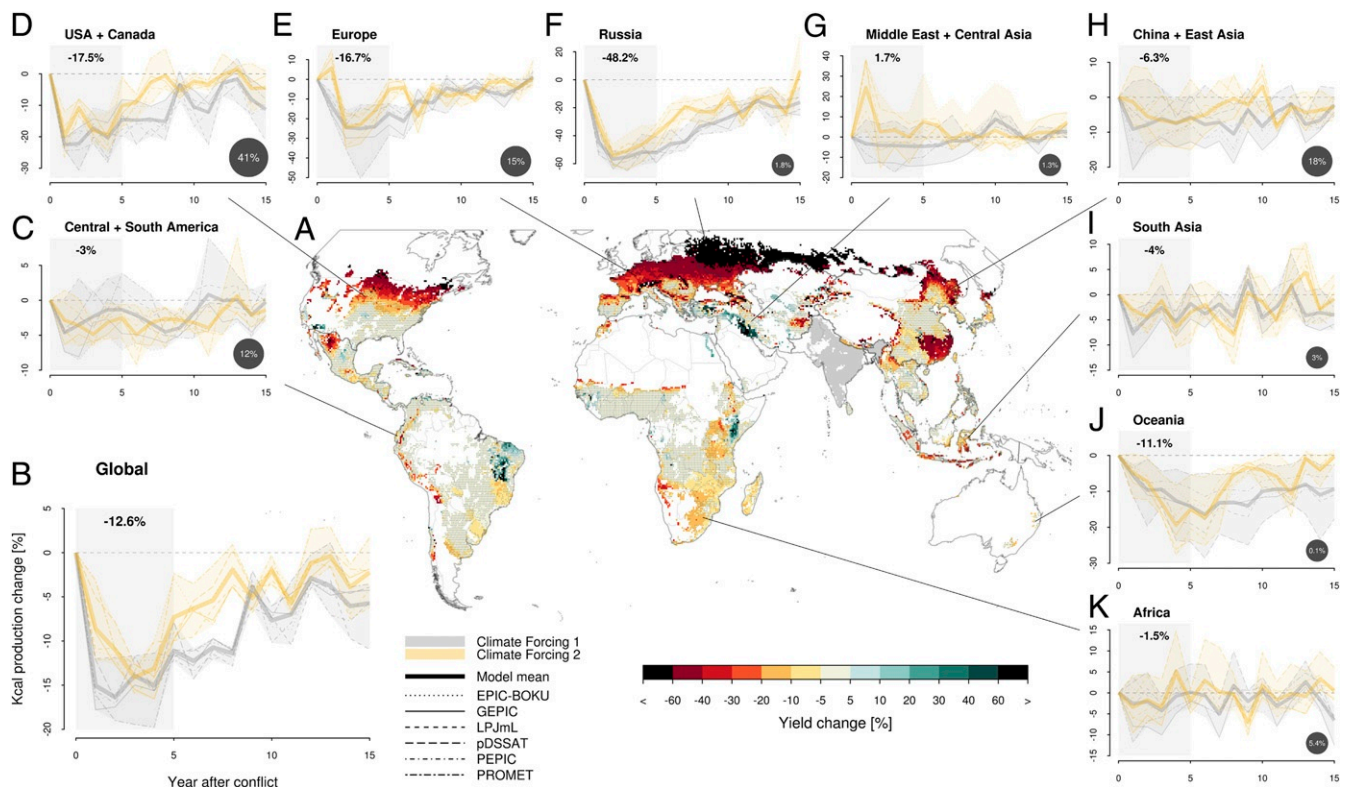
Fig. 3. Spatial and temporal patterns of maize impacts. (*A*) Relative maize yield changes (%) are shown as 5-y postconflict averages across the crop and climate model ensemble. (*B–K*) Time-series *Insets* illustrate aggregated changes in maize production (%) at (*B*) the global level and (*C–K*) nine world regions, for the participating crop models (line type), and two climate simulation sets (line color; climate forcing 1 [gray] and climate forcing 2 [yellow]), respectively. Mean years 1 to 5 production changes are highlighted on top of the shaded boxes. The contribution of each world region to global maize production is indicated in the bottom-right corner of the regional *Insets*. Grid cells (0.5°) with <10 ha maize harvested area are masked from the map (white) and hatching indicates cells in which not all crop models agree on the sign of simulated yield change. India and Pakistan are excluded.

source for wheat and rice. We find substantial differences in crop production impacts across uniformly perturbed historical years (i.e., each postconflict year of climate model anomalies is evaluated by the crop models across historical weather observations, from 1981 to 2009; *SI Appendix*, Fig. S1), with smallest relative impacts in below-average years (e.g., historic drought in 1988, an El Niño year) and largest relative and absolute impacts in favorable years (e.g., 1992) (*SI Appendix*, Fig. S7). For maize, the largest global loss across historical and postconflict years is 25% in 1992 and postconflict year 4 (*SI Appendix*, Table S4). The relative nature of the historical year has a larger influence on the response of global crop production than differences between the climate model ensemble simulations (CF1 and CF2, with three ensemble members each) for all crops but wheat, where both sources are comparatively small (*SI Appendix*, Fig. S11). There is no statistically significant trend in yield impacts over uniformly perturbed historical yields (*SI Appendix*, Fig. S7).

Global Trade Repercussions

Direct crop production losses after the nuclear conflict are concentrated primarily in the Northern Hemisphere, yet the shock is transmitted globally through international food trade. Indeed, the trade effects are especially severe as many of the most important cereal grain exporters are disproportionately impacted, including the United States, Canada, Europe, Russia, China, and Australia (23).

In the trade network analysis, countries respond to production losses by drawing on domestic food reserves, adjusting trade flows, and reducing domestic use, in that order. Reserves therefore serve to buffer the effect of production declines on a country's trade partners and domestic use. To better understand the impacts of the production declines, we combine the main simulation outputs—reserves and domestic use—into a key food security indicator known as the stocks-to-use ratio (STU), which is the country's food reserves relative to its domestic use.

The initial state of the food trade network is based on observed data of food production, trade, and reserves averaged from 2006 to 2008. Globally, the initial STU for maize and wheat is 0.20 (Fig. 6), meaning that reserves hold 20% of the world's annual demand (i.e., reserves could satisfy demand for 2.4 mo). Global initial reserves are higher for wheat (STU of 0.25) than for maize (STU of 0.16; *SI Appendix*, Figs. S12 and S13).

From this initial state, we track the repercussions of the production anomalies in the first 5 postconflict years using two networks, based on maize and wheat commodities separately (*SI Appendix*, Figs. S12 and S13; we focus on maize and wheat as their trade network results are more reliable; they contribute 69% of the export volume of the four crops studied; see *Materials and Methods*). In the first postconflict year, global reserves largely succeed in buffering the loss in production (both crops combined, Fig. 6). Food supply and trade demands stay near preconflict levels while global average STU for maize and wheat declines from 20 to 11%.

Maize reserves are largely depleted after year 1 in the majority of key exporting countries. Wheat reserves are largely depleted after year 2, further accelerating the propagation of the shock to the Global South. Continued production losses, mainly unbuffered after year 2, translate into reductions in domestic use of both crops (Fig. 6). By year 4, most major maize- and
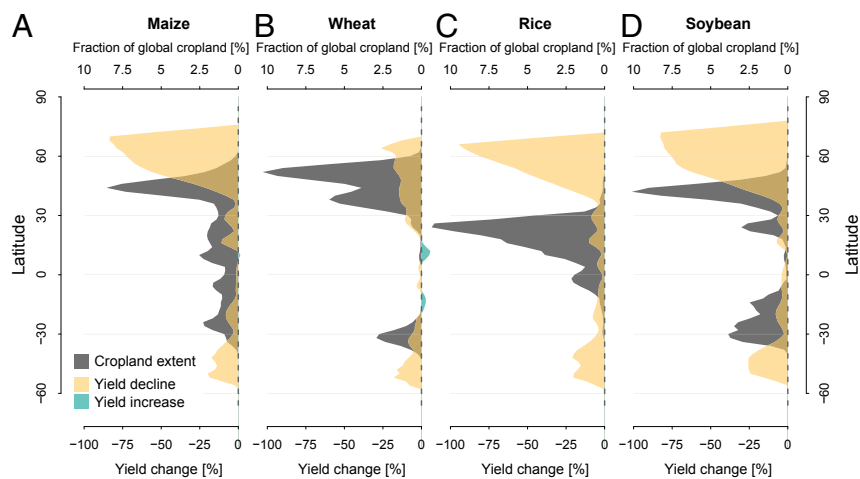
Fig. 4. Latitudinal profile of crop yield changes and cropland extent. Current cropland extent of the staple crops (*A*) maize, (*B*) wheat, (*C*) rice, and (*D*) soybean is shown across latitude bands as fractions of the crop-specific global extent (top *x* axis). Relative changes (5-y postconflict average) in crop yields are shown as latitude averages, based on rainfed crop simulations in all grid cells, unconstrained by current cropland areas (bottom *x* axis). The overlaps of gray and tan indicate areas with potentially adverse effects on current crop production. Yield data are presented as climate and crop model averages.

wheat-producing and trading countries—132 of 153 (combined population 5 billion people; *SI Appendix*, Table S3)—exhaust their reserves, and the global STU falls to 0.4%.

Even with reserve capacities and reduced exports, major exporting countries still experience substantial reductions in maize and wheat availability by the end of year 4, including Canada (−48% maize domestic use), Mexico (−26% maize), and Poland (−33% wheat). However, countries that rely heavily on imports to meet demand, many of which already face severe food insecurity, experience the largest constraints, including Libya (−69% wheat), Niger (−63% wheat), Somalia (−92% wheat), Rwanda (−75% wheat), Syria (−70% maize), Yemen (−37% wheat), Honduras (−39% maize), El Salvador (−38% maize), Haiti (−40% wheat), and Bangladesh (−41% wheat; *SI Appendix*, Tables S4 and S5). The United States, Brazil, and Argentina are among the few major countries that face losses in domestic maize and wheat use <3%, because high initial export shares are assumed to be reallocated to domestic use.

Globally, the reduction in domestic maize and wheat use increases from 1.2 to 13.0% between postconflict years 1 and 4, and the average reduction over the 5-y simulation period is 7.5%. The population in countries that face constraints to domestic use of >10% increases from 200 million in year 1 to 3.9 billion by year 4 (9 countries in year 1, 101 countries in year 4; *SI Appendix*, Table S3). A total of 1.3 billion (71 countries) and 600 million (45 countries) people live in countries that would face domestic use constraints of >20% and >30%, respectively, after year 4. Finally, crop production and food availability begin to recover in year 5 (*SI Appendix*, Figs. S12 and S13).

These results indicate the potential for a complete collapse in trade volumes, with all major exporters imposing bans on food exports. In the model, exports are banned when reserves are fully depleted, which is a conservative estimate as regulatory measures might be imposed earlier. Overall, the trade simulations suggest that current food stocks and international trade can largely buffer a sizable single-year anomaly, but persistent multiyear production losses would have severe implications for national food availability and thus food security.

Discussion

This study shows that a soot-induced sudden global cooling of about 1.8 °C would—for 5 to 10 y—be more harmful to global agriculture than the same amount of warming associated with

anthropogenic climate change (34, 35), as growth-enhancing effects of higher atmospheric CO_2 concentrations are lacking.

Large volcanic eruptions have led to historic famines—e.g., after Laki in 1783 to 1784 and the 1816 "year without a summer" after the Tambora eruption (9, 31)—but the cooling in each of the cases was < 1 °C and lasted only about 1 y (36). Sudden cooling by 1.8 °C from a limited nuclear war could cause 5-y average losses of >11% globally and >18% in the United States (up to 41% depending on the individual year in which the conflict occurs), which would exceed impacts during the Dust Bowl of the 1930s, the most severe period of droughts in recent US history (37). This study shows that 5-Tg soot emissions could trigger a severe food production shock, four times larger and more persistent than any recent extreme event since the beginning of the FAOSTAT record in 1961 (32). Depleting food reserves and trade dependencies would propagate the disruption to the Global South and reduce food availability in 71 countries by >20% and globally by 13%—suggesting that such food supply shock would have more severe societal implications than any other event documented in recent history.

The integrated simulation results indicate that this type of production shock would be experienced as a multiple-breadbasket failure. In contrast to local food system disruptions, such synchronized shocks potentially could not be alleviated by global trade or food aid as major export countries are hit hardest (24). Considering that smaller production shocks—as for instance in 2010, where wheat production fell by 33, 19, and 14% in Russia, Ukraine, and Canada, respectively (32)—are often associated with commodity price surges, critical spikes in global food prices could ensue, particularly in view of the multiyear nature of this anomaly. Inflated food prices can exacerbate inequalities and social unrest, especially in developing countries (38).

Current grain reserves are shown to largely be depleted within 1 y after the conflict, which results in vulnerabilities of national food supplies in subsequent years. The trade network analysis is based on the average crop production response across 29 historical years, meaning that individual years can cause larger losses (*SI Appendix*, Fig. S7) and potentially put additional stress on the global food system. More generally, the model captures critical cascading effects of a food production shock with a short-term, nonlinear, and out-of-equilibrium response often not addressed in equilibrium-based integrated
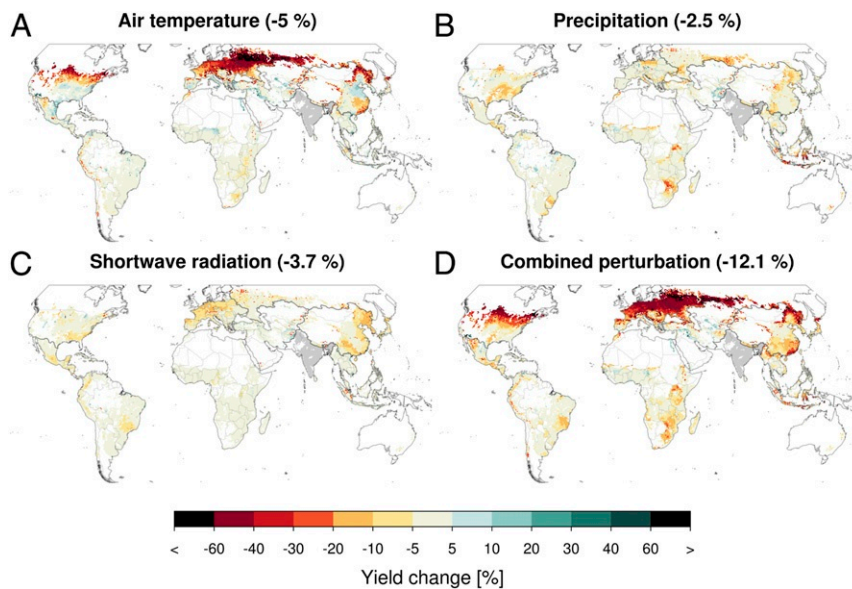
Fig. 5. Maize yield and production sensitivity to individually perturbed climate drivers. Changes in simulated maize yield (%) for climate input variables perturbed one at a time: (*A*) air temperature, (*B*) precipitation, and (*C*) surface incoming shortwave solar radiation, filled in with control AgMERRA climate. (*D*) The combined perturbation has all four drivers perturbed collectively. Percentage numbers at the top of each plot indicate the respective global caloric production change. This sensitivity study is performed for climate model simulation CF1$_a$ and by the crop models EPIC-BOKU, GEPIC, LPJmL, pDSSAT, and PEPIC. Data are shown as the mean across crop models, post conflict years 1 to 5, 29 y of historical climatology, and rainfed and irrigated systems. India and Pakistan are excluded.

assessment model approaches. While our results provide evidence for substantial reductions in national food availability after a persistent multiyear anomaly, characterizations of reductions in specific per capita food consumption or human health impacts require more detailed considerations of local economic conditions, food access, and nutrition. Nevertheless, it is likely that national trade restrictions to stabilize domestic markets and price spikes would spread and compound international market instability (39), thereby aggravating food shortages in resource-poor communities and potentially triggering additional hunger and other adverse human health implications around the world.

Crop model results are in line with previous provisional estimates under a similar 5 Tg soot scenario (20, 22), also confirming that irrigated systems are more resilient—this study provides a comprehensive global multimodel assessment across major crops (six different crop models and two different climate model configurations), critical for evaluating economic ramifications. Yield losses are attributed to anomalies in temperature, precipitation, and radiation. Lower temperatures affect crop growth directly by slowing phenological development, reducing photosynthetic activity, damaging tissue, and reducing root growth; indirect effects can occur via for instance water stress, nitrogen cycling, and snow cover. Crop development is slower in cooler weather, and crop models demonstrate that the temperature anomaly extends current growing periods to the point that higher-latitude crops fail to reach physiological maturity (*SI Appendix*, Fig. S9). Longer growing periods also increase the risk of frost exposure. Direct frost damage, however, is currently not considered in all global crop models, which contributes to uncertainties (*SI Appendix*, Table S1). Overall, despite differences in responses to individual climate drivers, the ensemble of crop models agrees on an estimate of crop responses at a global level (*SI Appendix*, Fig. S8).

Soot injections lead to higher stratospheric temperatures, which in turn would cause stratospheric ozone depletion (8, 16). Since ozone strongly absorbs UV radiation, soot injection leads to enhancement of UV levels at the land surface, espe-

cially poleward of 20°N and S (15, 16), with additional hazards to agriculture and human health (4, 5). Increased UV is shown to reduce plant growth rates, but also to improve crop quality and pest resistance (40). The large-scale net effect remains unclear and as of yet no models have been developed to simulate mechanistic UV effects on cereal yield and quality (41). Surface ozone is likely to deplete as well, which can reduce surface ozone damage to crops (42), an effect not considered here. On the other hand, observations show that plant canopies use diffuse radiation more efficiently than direct sunlight (43). Increased diffuse light due to sooty aerosols may therefore partially offset reductions in insolation, but the global gross significance of this complex relationship remains unresolved (44, 45). CO_2 emissions from the ensuing fires are considered marginal at the global level (1) and its atmospheric concentration in the crop models is thus held constant over the simulation period. Other yield-limiting factors due to social disruptions—including shortages of labor, fuel, fertilizer, and seeds, but also the nutritional value of crops—are not considered here, and have the potential to further reduce crop production and quality.

Adaptation potentials to the climate anomalies studied here include switching to faster-maturing crop varieties or other crops that tolerate lower temperatures and radiation levels [e.g., potatoes or beets instead of cereal grain (46)]. These could help alleviate production shocks in subsequent growing seasons, but seed and infrastructure availability and farming system knowledge might be limiting factors for ad hoc implementation at a large scale (18). If water availability allows, supplemental irrigation could stabilize yields in regions with precipitation declines such as in parts of the United States and the North China Plains, and cutting allocations for biofuel and feed crops could provide additional opportunities especially at lower latitudes. A precautionary building of larger food stockpiles is controversial but might increase the buffer in the first year after the production disruption. While a coordinated effort by countries with large reserves (e.g., >3 mo worth of their own domestic use) for strategic releases could play a stabilizing role in the global food system, there is no plan for major food-producing countries
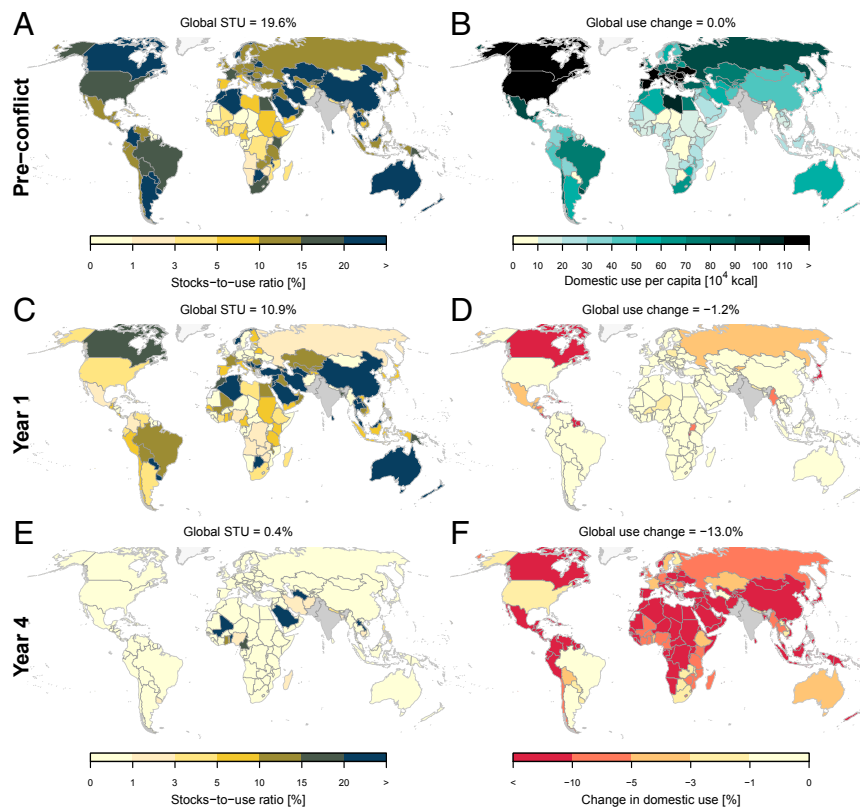
Fig. 6. Initial and postconflict food reserves and domestic use. For maize and wheat combined, stocks-to-use ratios (%)—food reserves relative to domestic use—are shown at the country level for (*A*) current conditions (2006 to 2008 average), (*C*) the postconflict year 1, and (*E*) postconflict year 4. *B*, *D*, and *F* show maize and wheat domestic use, as (*B*) absolute preconflict kilocalories per capita and (*D* and *F*) relative postconflict changes (%) for (*D*) year 1 and (*F*) year 4, which is the year with largest declines (*SI Appendix*, Figs. S12 and S13). The trade network analysis evaluates national caloric crop production changes averaged across crop and climate models, but individually for each crop (without substitution between crops). India and Pakistan are excluded.

to proactively intervene in response to a multiple-breadbasket failure (23).

We employed a case with 5 Tg of soot that has been evaluated in several climate models producing similar results (16, 31). Besides the South Asia case evaluated here, other nuclear conflicts are possible (13). Recent CESM simulations successfully reproduced observed soot lofting and transport in the stratosphere after the 2017 forest fires in Canada, providing observational evidence and validation for some of the assumptions in the climate simulations used herein (6). The season and geographic location of soot emissions could influence soot production, rainout, and lofting, yet a systematic evaluation is lacking (6, 15). The size of the conflict, fuel load, smoke composition, and plume rise introduce additional uncertainties (6, 8, 15, 17, 31, 47, 48). Recently revised estimates of combustible material with today's larger nuclear arsenals render previous assumptions of 5 Tg soot conservative and suggest that soot production may range from 5 to 36 Tg for the India–Pakistan case (13). Climatic responses are shown to proportionally increase with higher soot emissions and our findings suggest a linear crop yield decline across local temperature reductions between −1.5 and −4 °C (*SI Appendix*, Fig. S10).

Yield impacts across uniformly perturbed historical years do not reveal a statistically significant trend (*SI Appendix*, Fig. S7) despite the underlying increase in global mean temperature, suggesting that a conflict shifted into the near future would likely result in similar crop responses. The relative temperature anomaly would be similar even under additional global warming and crop cultivars are expected to be adapted to warmer growing periods in the future (49), likely leading to somewhat comparable

crop responses. However, our results would not necessarily apply several decades into the future, where regional impacts might be different due to local rainfall and temperature changes with unabated climate change. Recently, systematic warming experiments with the same GGCMI models used here show that crop yields—at global average level and without cultivar adaptation—also decline under positive local temperature change exceeding 0.5 to 1 °C (50, 51). This global signal entails high-latitude gains under moderate warming and substantial losses in the tropics, complementing the picture we find here under colder temperatures. Using artificial stratospheric aerosols to reduce global warming has been suggested as a climate intervention (geoengineering) strategy (52). While such solar radiation management is associated with many other risks still poorly understood (45, 53), potentially viable options for deployment would use sulfate aerosols, not soot. Soot would, besides other risks, cause ozone destruction (54).

In conclusion, a robust signal across climate and crop models suggests that even a limited nuclear war could substantially impair staple crop production with 20 to 50% losses above 30°N, or 11% globally, on average for 5 y after the conflict. Such persistent production anomalies are shown to exceed those caused by historic droughts and volcano eruptions. This study provides evidence that current global food reserves and trade cannot avert ensuing constraints to domestic food availability; domestic use of maize and wheat is shown to decline by >10% in countries with a total population of 3.7 billion inhabitants. Food system implications of a regional nuclear war unfold globally, with the largest impacts on countries that are main food producers.

Jägermeyr et al.

Materials and Methods

Experimental Design. To investigate indirect implications of a nuclear conflict on global food supply, we use two previously published climate model simulation sets that evaluate both fire-related soot emissions of 5 Tg and resulting climate perturbations using well-established Earth system models with interactive coupling of the atmosphere, land, ocean, and sea ice (13, 15). We calculate climate simulation anomalies to perturb an observational historical weather dataset to generate a bias-free and high-resolution weather dataset for global crop modeling. Each postconflict year of climate forcing is used to perturb 31 y of historical weather data, respectively, to sample interannual differences (only 29 y are analyzed; see below). Six leading global process-based crop models use this set of the weather perturbations to run simulations for the four major staple crops: maize, wheat, rice, and soybean. In addition, climate sensitivity runs in which climate drivers are perturbed one at a time are performed to identify the crop response to each driver individually (temperature, precipitation, and short- and longwave radiation). To represent realistic geographic crop production patterns, we combine simulated fractional crop yield changes with spatially explicit yield observations. Aggregated country-level production anomalies simulated by the crop models are then introduced into a food trade network to assess global effects on food reserves and domestic use (see *SI Appendix*, Fig. S1 for an overview of the simulation protocol).

Nuclear Conflict Scenario. The first climate model simulation set (henceforth CF1) uses a simple set of assumptions involving 100 Hiroshima-sized detonations of 15 kt yield on the most populated urban areas in India and Pakistan (31, 47). Each detonation is assumed to burn an area of 13 km^2, and based on detailed quantification of combustible material in the target regions, this scenario injects ∼5 Tg of soot aerosol particles into the upper troposphere at 150 to 300 hPa. After assuming that 20% of the soot rained out below 300 hPa, it is injected uniformly over a broad area over Pakistan and northern portions of India (15, 47). The soot particles are assumed to be monodisperse and are not allowed to coagulate. After emission, an additional 10 to 15% of the soot rains out from the upper troposphere as the remainder is lofted into the stratosphere (15, 47). This low rainout efficiency based on inefficient removal of small, fresh smoke particles is supported by observations of convection associated with forest fires (55).

To explore the sensitivity of the climate model simulations to assumptions about aerosols and soot emissions, we consider a second climate model simulation set (CF2) using the same total amount of tropospheric soot emission, but based on targets using updated fuel loads and an updated climate model version (13). Here only forty-four 15-kt weapons result in 5 Tg of soot, again assuming 20% initial removal in the troposphere. In contrast to CF1, the smoke injections are spatially explicit at the target location and spread over a period of 4 d (6 at day 0, 16 at day 1, 16 at day 2, 6 at day 3) (13). Soot is represented as fractal particles that are allowed to coagulate, forming larger particle sizes, which can fall out faster than the smaller particles in CF1. As they are fractals, they have smaller fall velocities and more absorption than spherical particles with a comparable mass. Similar to CF1, a significant fraction of the soot is rained out in the upper troposphere as the remainder is lofted into the stratosphere.

The assumptions herein have been investigated by multiple studies (8, 13, 15, 31) and systematically evaluated by Stenke et al. (16), who simulated 1- to 12-Tg soot emissions. Recently refined calculations of combustible material with today's larger arsenals and higher population densities render previous assumptions of 5 Tg soot as the lower end of estimates. Toon et al. (13) suggest emission of 5 to 36 Tg soot for the India–Pakistan case, depending on assumptions of weapon yield. To be consistent with CF1 and to evaluate effects of different aerosol treatment, we here focus on the 5 Tg case.

Climate Model Simulations with 5 Tg Soot Emission. Both CF1 and CF2 simulation sets are previously published (13, 15), but for clarity we provide a brief methods description here. Soot is injected into the upper troposphere over the Indian subcontinent on 15 May 2013 (CF1) and 15 May 2000 (CF2). Simulations run 26 (CF1) and 15 (CF2) transient years postconflict, using carbon dioxide concentrations according to RCP 4.5 (CF1) and fixed values at year 2000 levels (CF2) (13, 15). Both CF1 and CF2 performed three model realizations based on different initial conditions (Fig. 1, runs a–c).

Climate simulations for CF1 and CF2 were performed with NCAR's CESM, a state-of-the-art, fully coupled, global climate model, configured with fully interactive ocean, land, sea ice, and atmospheric components (25). The atmospheric component is represented by the Whole Atmosphere Community Climate Model, version 4 (WACCM). WACCM is a high-top chemistry–climate model that extends from the surface to 5.1×10^6 hPa (∼140 km). It has 66 vertical levels and spatial resolution of 1.9° latitude × 2.5° longitude.

WACCM includes interactive chemistry that is fully integrated into its dynamics and physics (15). To represent the evolution of smoke injection more accurately, the CF2 simulations are based on a WACCM version with advanced stratospheric aerosol microphysics by being coupled with the Community Aerosol and Radiation Model for Atmospheres (56). CARMA is a sectional aerosol parameterization that resolves the aerosol size distribution and allows it to evolve freely [more details in Toon et al. (13)].

Smoke emission, rainout, injection height, and self-lofting into the stratosphere can vary by season and geographic location. Previous studies that inject smoke only into the upper troposphere and lower stratosphere indicate that the seasonality of soot injection might not fundamentally affect the global multiyear climate response (6), but there is no systematic assessment yet.

Overall, the WACCM model framework is well established and evaluated and has been used for instance to successfully simulate the climate and atmospheric chemistry after the asteroid impact that caused the extinction of the dinosaurs 66 million y ago (57), and it successfully reproduced the observations from soot lofting of smoke injected by pyrocumulonimbus clouds after the 2017 Canadian wildfires (6).

Climate Perturbation Protocol for Crop Model Simulations. We use the daily bias-adjusted climate forcing dataset AgMERRA (Agricultural applications version of the Modern-Era Retrospective Analysis for Research and Applications, 1980 to 2010) (26) both for control simulations and for constructing the perturbation climatology (see below). AgMERRA is designed for analyzing agricultural impacts related to climate variability and climate change with global coverage. It is derived from the NASA Modern-Era Retrospective analysis for Research and Applications (MERRA). We use the following daily climate variables at 0.5° spatial resolution: mean, minimum, and maximum 2-m air temperature (T, $Tmin$, and $Tmax$, respectively [°C]), precipitation (P [mm/d]), and shortwave and longwave radiation (SR and LR [W/m^2]). LR is not provided by AgMERRA and substituted with an alternative from the WFDEI product (WATCH forcing data [WFD] methodology applied to the ERA-Interim [EI] reanalysis) (58).

For each postconflict year of the six climate model simulations (CF1$_{a-c}$, CF2$_{a-c}$) we extract monthly anomalies for the four climate variables to perturb the 31-y historical AgMERRA dataset (*SI Appendix*, Fig. S1). This "delta shifting" is done for three reasons: 1) Higher spatial resolution improves crop model simulations; 2) each year of the nuclear conflict perturbation (26 and 15 y for CF1 and CF2, respectively) is simulated for 31 historical years individually, which allows addressing interannual differences across historical years perturbed with identical climate forcing; and 3) no bias adjustment is required and we maintain the observed weather variability of AgMERRA. Representing natural variability in the weather input is critical for reliable crop yield estimates (27). The monthly delta-shifting approach neglects potential changes in daily climate variability. However, the SD of daily temperature and precipitation in perturbed postconflict climate model simulations is virtually unchanged compared to that in the control climate simulations, which supports the delta-shifting approach and suggests that we are not missing potentially adverse additional effects due to increased daily variability in the climate model simulations.

This setup creates 3 × 26 (CF1$_{a-c}$) and 3 × 15 (CF2$_{a-c}$) individual simulations, each with 31 transient years of perturbed AgMERRA data. In favor of simulating multiple historical years for the same climate anomaly, the simulation protocol entails transient historical simulations separately for each postconflict year (*SI Appendix*, Fig. S1), which neglects carryover effects between postconflict years. Those are, however, expected to be less important than the carryover effects between historical transient simulations. The first and last years of the transient runs are removed from crop model simulations due to partially incomplete growing seasons.

The anomaly forcing term for temperature (ΔT, calculated individually for T, $Tmin$, and $Tmax$) is the absolute difference between climate model control ($Tcon$) and perturbation ($Tper$) in each grid cell c, postconflict year y, and month m:

$$\Delta T_{y,m,c} = Tper_{y,m,c} - Tcon_{y,m,c}. \qquad [1]$$

ΔT is then added to the daily control AgMERRA time series to create the delta-corrected product (TAG) with constant perturbation across all 31 AgMERRA years (a):

$$TAG_{y,a,m,c} = TAG_{a,m,c} + \Delta T_{y,m,c}. \qquad [2]$$

Jägermeyr et al.

Forcing terms for *P*, *SR*, and *LR* are calculated as relative changes, such as

$$\Delta SR_{y,m,c} = \frac{SRper_{y,m,c}}{SRcon_{y,m,c}}. \qquad [3]$$

For precipitation, *PRcon* is the multiyear average control climatology to reduce interannual variability. The *P*, *SR*, and *LR* Δ term is then multiplied with the daily control AgMERRA time series:

$$SRAG_{y,a,c} = SRAG_{a,m,c} \times \Delta SR_{y,m,c}. \qquad [4]$$

Net longwave radiation for use in the LPJmL model is calculated from *T* [K] and *LR*, using the Stefan–Boltzmann equation, assuming emissivity is 1:

$$LRnet = (5.670373 * 10^{-8} \times T^4) - LR. \qquad [5]$$

The PROMET model requires subdaily weather data and therefore uses ERA-Interim instead of AgMERRA data. Since we use crop yield anomalies from each model separately (see below), the differences between AgMERRA and ERA-Interim are not expected to influence the overall crop model postconflict yield estimates.

Crop Yield Simulations. Six gridded global crop models participated in this study: EPIC-BOKU (59), GEPIC (60), LPJmL (61), pDSSAT (62, 63), PEPIC (64), and PROMET (65, 66), as part of the GGCMI (28, 29) within the Agricultural Model Intercomparison and Improvement Project (AgMIP) (67). Although some models have descended from the same parent model, different parameterization and subroutine selections render each contribution independent (68). We focus on the four major global grain crops, that is, maize (*Zea mays* L.), wheat (*Triticum* sp. L.), rice (*Oryza sativa* L.), and soybean (*Glycine max* L. Merr.). Wheat is simulated as winter and spring wheat individually; grain and silage maize are not distinguished. Together these crops contribute 90% of today's global caloric production of all cereals (32); herein cereals include soybean. All crop models simulate the four crops under both rainfed and irrigated conditions in each grid cell irrespective of current land-use patterns. The physical cropland extent, including irrigated fractions, is applied in the postprocessing based on the MIRCA2000 (Monthly Irrigated and Rainfed Crop Areas around the year 2000) reference dataset (69) and is held constant over time. Crop production is calculated as yield times harvested area of the respective crop. We omit grid cells with <10 ha cropland area for each crop. All simulations are carried out at the 0.5° global grid.

Crop models are harmonized for 1) planting and maturity dates as in GGCMI phase 2 (51), 2) spatially explicit fertilizer input as in Elliott et al. (29), and 3) unconstrained water availability for irrigation (29). The latter assumes that under irrigation any soil water deficit is practically eliminated the next day and no conveyance or application losses are withheld. PROMET simulates potential yields without fertilizer constraints. Soil moisture and soil temperature for various soil layers are calculated by the crop models in a transient way, that is, without reinitializing at the beginning of each year. All models use a classic phenological heat sum approach to determine physiological stages (respective base temperatures are listed in *SI Appendix*, Table S1) between planting and maturity. Heat unit accumulation can be modified by the sensitivity to day length (photoperiod) and for winter wheat it is stalled until vernalization requirements are reached, that is, the exposure to cold temperatures before reaching anthesis. Planting dates are constant across all simulations but the heat sum approach leads to later maturity dates in colder years. Simulated growing seasons shorter than 50 d result in the assumption of crop failure. We simulate only one growing season per calendar year, and since two harvests can occur within the same calendar year (e.g., in regions where harvests are close to the end of year), we report growing seasons in sequence and not by the calendar year (29). This may cause disagreement with the reporting of the UN's FAOSTAT, where harvest seasons are assigned to the calendar year in which the majority of the harvest happens. Time series correlation between simulations and FAOSTAT statistics can therefore be affected, but it occurs only in a small number of grid cells and it does not affect the simulated SD of yield time series or simulated postconflict yield impacts (68). To avoid temporal trends in crop simulations, all model inputs (including land use, atmospheric carbon dioxide concentrations, NO_3 and NH_4 deposition rates, and crop cultivars) except weather are held constant at year 1995 levels, the center of the 1980 to 2010 simulation period. We are not accounting for additional CO_2 emissions from fires as they are considered negligible compared to the global budget (1, 13).

Except LPJmL and PEPIC, which are adjusted to match national yield observations [1998 to 2007 (32)], none of the models accounts for human management intervention other than fertilizer application, irrigation, seed selection, and growing periods. To represent realistic crop production estimates, we calculate fractional yield changes from each individual crop model between the control and perturbation scenarios and apply these to a spatially explicit (0.5°) observational yield reference dataset representative for the time period 2003 to 2007 (*SI Appendix*, Fig. S14). SPAM2005 (Spatial Production Allocation Model 2005) (70) is used as the main reference yield data as it separates rainfed and irrigated systems. Grid cells with missing SPAM2005 yield data but with >10 ha MIRCA2000 harvested area are gap filled with Ray et al. (71) yield data; both SPAM2005 and Ray et al. (71) represent the time period 2003 to 2007.

Historical maize yield ensemble simulations agree well with observations, especially during extreme years such as 1983, 1988, and 2004 (*SI Appendix*, Fig. S7). The observed and simulated yield range and variability are well in agreement (observed and simulated SDs are 0.187 and 0.181 t/ha, respectively), and the ensemble mean often reproduces observations better than any individual crop model (*SI Appendix*, Fig. S15), which underpins the utility of the ensemble. While the models reliably reproduce yield declines in extreme years, they cannot account for flooding events, which partly explains, for example, the disagreement in 1993 (*SI Appendix*, Fig. S7). Additional evaluation of model performances is presented in *SI Appendix*, Fig. S15 and more thoroughly by Müller et al. (68).

Each model reacts differently to cold temperatures with associated effects on phenological development, crop growth, grain filling, and physical damage (see *SI Appendix*, Table S1 for an overview). In pDSSAT grain filling is terminated prior to physiological maturity after 5 consecutive days with insufficient kernel growth rate, which is the case if $T < Tbase$, the phenological base temperature (63). Additionally, cold temperature mortality defaults to –25 °C, which affects only wheat. PROMET considers frost killing if temperatures fall below –8 °C, except for winter wheat. Frost killing is not considered during germination and after reaching physiological maturity. Crop failure is assumed if air temperature falls below the crop-specific base temperature on more than 14 consecutive days (66). All EPIC-based models consider biomass reduction for winter crops, depending on crop-specific frost sensitivity and base temperature. They also account for frost damage, depending on the snow cover. LPJmL and PROMET consider a maximal length of the growing period at which early harvest is enforced, irrespective of physiological maturity (*SI Appendix*, Table S1). GEPIC and PEPIC enforce early harvest on 1 December (Northern Hemisphere) and 1 June (Southern Hemisphere). See *SI Appendix*, Table S1 for additional crop model-specific details on response mechanisms to cold temperatures.

Wheat, and winter wheat in particular, shows larger uncertainty in the crop model response to the simulated climate perturbation compared to maize and soy (Fig. 2 and *SI Appendix*, Figs. S3 and S4). In large part, this is due to 1) whether vernalization is considered in a specific model and 2) if so, the calibration of vernalization parameters is difficult for global simulations; 3) whether frost damage is considered and 4) if so, the calibration of frost damage parameters can be cultivar specific and therefore difficult to generalize for a global study; and 5) the effect of snow cover on effective temperature. Each of these aspects is handled differently in the models, but is particularly relevant for winter wheat.

EPIC-BOKU cannot provide growing season outputs, and therefore GEPIC and PEPIC results are used to identify cells with crop failures due to excessive growing season length. GEPIC and EPIC-BOKU use the Hargreaves method to estimate potential evapotranspiration (59), while PEPIC uses the Penman–Monteith method (64). All EPIC-based models use the same core executable (EPICv0810) but differences arise from parameterizations of crop cultivars, soil attributes, soil nutrient cycling, hydrologic processes, and field management. See Folberth et al. (72) for additional details and evaluations.

We calculate crop yield anomalies for simulated and observed data as detrended (first quadratic polynomial subtracted) and normalized (mean subtracted) yields based on the entire data record (i.e., simulated yields 1981 to 2009 and observed yields 1961 to 2017). Explained variances (R^2, in percent) are based on the Pearson correlation coefficient derived from simulated and observed [FAOSTAT (32)] national yield time series and to quantify residuals we calculate root-mean-square errors.

Food Trade Network. To simulate the global repercussions of the nuclear conflict-induced food production shock, we use an observational representation of the global food trade network at the country level (30). Therein, reduction of national food production is partly absorbed through decreases in domestic reserves and use and partly transmitted through the adjustment of trade flow. Through adjustments to trade flows, the effects of the initial production shock propagate through the global system. Observed data

Jägermeyr et al.

from FAOSTAT (32) and the US Department of Agriculture (73) for maize and wheat in caloric equivalents of food production, reserves, and trade are averaged from 2006 to 2008 to create a baseline food trade network into which we introduce simulated crop production anomalies [see Marchand et al. (30) for more details].

For each country i in the analysis, we define the net supply (S_i) of a food commodity for a given year (y) as

$$S_{i,y} = Pr_{i,y} + Im_{i,y} - Ex_{i,y}, \qquad [6]$$

where Pr is domestic production, Im is the sum of all imports, and Ex is the sum of all exports. Next, we define a change in a country's reserves (ΔR) over the same time period as

$$\Delta R_{i,y} = S_{i,y} - U_{i,y}, \qquad [7]$$

where U is defined broadly as domestic use, including any food wasted. To avoid misinterpretation, we use the term "domestic use" instead of "domestic consumption," used in the original publication of the trade network (30). The simulated changes in domestic use are based on generalized assumptions to fulfill network dependencies and are indicative of constraints to national inventories but should not be interpreted as reductions in individual per capita consumption or potential undernourishment.

Negative values of ΔR mean that reserves are used, while positive values mean that surplus amounts of a commodity are transferred to storage. Finally, we define the overall national food commodity inventory (I) as

$$I_{i,y} = S_{i,y} + R_{i,y}. \qquad [8]$$

The trade network is evaluated annually, as crop production anomalies are at the annual time step. Negative crop production anomalies are absorbed by first using reserves. If depleted, imports are increased, exports are blocked, and domestic use is reduced. The simulation ends when all countries—through reserves, consumption, and trade—are able to absorb their supply shocks caused by production decreases and trade demands. We run the trade network analysis for the first 5 postconflict years, based on average crop production anomalies across the 29 historical years (*SI Appendix*, Fig. S1).

STUs, calculated as a country's reserves relative to initial domestic use,

$$STU_{i,y} = \frac{R_{i,y}}{S_{i,initial}}, \qquad [9]$$

provide an indication of the resilience of a country and the global food system to such decreases in production. Comparing the change in STU pre- and postconflict captures how different the postshock equilibrium is from the initial state as a result of decreases to reserves around the world (Fig. 6 and *SI Appendix*, Table S3). With decreases in reserve stocks, which buffer the effects of production declines, future production decreases will be increasingly absorbed through trade, thus affecting more countries, and through decreases in domestic use.

We focus the food trade network analysis on maize and wheat as they are the two most important staple crops contributing 69% (2006 to 2008) of the combined exports of the four crops studied (32). These two crops have the most reliable observational data available and thus the model of trade and reserve dynamics is most robust. India and Pakistan are excluded from the trade network by assuming zero imports and export, to avoid arbitrary assumptions on changes in food production and demand and to be consistent with the remaining analyses in this study (see *SI Appendix*, Table S2 for crop production changes under different assumptions). Yet, removing India and Pakistan from the initial observation-based trade dependencies creates reduced import availability in countries that exhibit trade connections with India and Pakistan. This effect, however, is more important for rice as South Asia is a large rice exporter. Country population is taken from the Natural Earth product (74) representing the year 2017 (*SI Appendix*, Table S3).

The trade network analysis assumes constant food demand over time, and maize and wheat are evaluated separately without substituting between crops. The representation of the livestock sector and food prices is beyond the scope of this study. Exports are banned when reserves are fully depleted, which is a conservative estimate as some countries might impose regulatory measures to stabilize domestic markets earlier. The network does not include such political decisions, including panic buying, precautionary purchases, and other behavioral responses that would amplify nonlinearities in the response of the global food trade system. However, the network is grounded in national observed inventories and reproduces supply and demand trade flow dynamics (30). It captures critical interdependencies among countries and provides a framework to study the short-term, nonlinear, and out-of-equilibrium response of trade networks to supply shocks.

1. P. J. Crutzen, J. W. Birks, The atmosphere after a nuclear war: Twilight at noon. *Ambio* **11**, 114–125 (1982).
2. R. P. Turco, O. B. Toon, T. P. Ackerman, J. B. Pollack, C. Sagan, Nuclear winter: Global consequences of multiple nuclear explosions. *Science* **222**, 1283–1292 (1983).
3. C. Sagan, Nuclear war and climatic catastrophe: Some policy implications. *Foreign Aff.* **62**, 257 (1983).
4. P. R. Ehrlich *et al.*, Long-term biological consequences of nuclear war. *Science* **222**, 1293–1300 (1983).
5. M. A. Harwell, T. C. Hutchinson, W. P. J. Cropper, C. C. Harwell, H. D. Grover, "Environmental consequences of nuclear war" in *Ecological and Agricultural Effects*, R. E. Munn, Ed. (Wiley, New York, NY, 1985), vol. 2.
6. P. Yu *et al.*, Black carbon lofts wildfire smoke high into the stratosphere to form a persistent plume. *Science* **365**, 587–590 (2019).
7. O. B. Toon *et al.*, Consequences of regional-scale nuclear conflicts. *Science* **315**, 1224–1225 (2007).
8. M. J. Mills, O. B. Toon, R. P. Turco, D. E. Kinnison, R. R. Garcia, Massive global ozone loss predicted following regional nuclear conflict. *Proc. Natl. Acad. Sci. U.S.A.* **105**, 5307–5312 (2008).
9. R. B. Stothers, The great Tambora eruption in 1815 and its aftermath. *Science* **224**, 1191–1198 (1984).
10. S. Ganguly, M. Smetana, S. Abdullah, A. Karmazin, India, Pakistan, and the Kashmir dispute: Unpacking the dynamics of a South Asian frozen conflict. *Asia Eur. J.* **17**, 129–143 (2019).
11. P. Pulla, India–Pakistan nuclear escalation: Where could it lead?. *Nature* **573**, 16–17 (2019).
12. R. W. Khan, F. H. French, "South Asian stability workshop: A crisis simulation exercise" (Rep. 2013-008, Project on Advanced Systems and Concepts for Countering weapons of mass destruction (PASCC), Naval Postgraduate School Center on Contemporary Conflict and Defense Threat Reduction Agency, Colombo, Sri Lanka, 2013).
13. O. B. Toon *et al.*, Rapidly expanding nuclear arsenals in Pakistan and India portend regional and global catastrophe. *Sci. Adv.* **5**, eaay5478 (2019).
14. A. Robock, L. Oman, G. L. Stenchikov, Nuclear winter revisited with a modern climate model and current nuclear arsenals: Still catastrophic consequences. *J. Geophys. Res. Atmos.* **112**, 1–14 (2007).
15. M. J. Mills, O. B. Toon, J. Lee-Taylor, A. Robock, Multidecadal global cooling and unprecedented ozone loss following a regional nuclear conflict. *Earth's Future* **2**, 161–176 (2014).
16. A. Stenke *et al.*, Climate and chemistry effects of a regional scale nuclear conflict. *Atmos. Chem. Phys.* **13**, 9713–9729 (2013).
17. F. S. R. Pausata, J. Lindvall, A. M. L. Ekman, G. Svensson, Climate effects of a hypothetical regional nuclear war: Sensitivity to emission duration and particle composition. *Earth's Future* **4**, 498–511 (2016).
18. K. C. Engvild, A review of the risks of sudden global cooling and its effects on agriculture. *Agric. For. Meteorol.* **115**, 127–137 (2003).
19. T. R. Sinclair, Simulated soya bean production during the recovery phase of a nuclear winter. *Agric. Ecosyst. Environ.* **17**, 181–185 (1986).
20. M. Özdoğan, A. Robock, C. J. Kucharik, Impacts of a nuclear war in South Asia on soybean and maize production in the midwest United States. *Climatic Change* **116**, 373–387 (2013).
21. L. Xia, A. Robock, Impacts of a nuclear war in South Asia on rice production in mainland China. *Climatic Change* **116**, 357–372 (2013).
22. L. Xia, A. Robock, M. Mills, A. Stenke, I. Helfand, Decadal reduction of Chinese agriculture after a regional nuclear war. *Earth's Future* **3**, 37–48 (2015).
23. M. J. Puma, S. Bose, S. Young Chon, B. I. Cook, Assessing the evolving fragility of the global food system. *Environ. Res. Lett.* **10**, 024007 (2015).
24. S. D. Baum, D. C. Denkenberger, J. M. Pearce, A. Robock, R. Winkler, Resilience to global food supply catastrophes. *Environ. Syst. Decis.* **35**, 301–313 (2015).

25. J. W. Hurrell *et al.*, The Community Earth System Model: A framework for collaborative research. *Bull. Am. Meteorol. Soc.* **94**, 1339–1360 (2013).

26. A. C. Ruane, R. Goldberg, J. Chryssanthacopoulos, Climate forcing datasets for agricultural modeling: Merged products for gap-filling and historical climate series estimation. *Agric. For. Meteorol.* **200**, 233–248 (2015).

27. M. Glotter *et al.*, Evaluating the utility of dynamical downscaling in agricultural impacts projections. *Proc. Natl. Acad. Sci. U.S.A.* **111**, 8776–8781 (2014).

28. C. Rosenzweig *et al.*, Assessing agricultural risks of climate change in the 21st century in a global gridded crop model intercomparison. *Proc. Natl. Acad. Sci. U.S.A.* **111**, 3268–3273 (2014).

29. J. Elliott *et al.*, The Global Gridded Crop Model Intercomparison: Data and modeling protocols for phase 1 (v1.0). *Geosci. Model Dev.* **8**, 261–277 (2015).

30. P. Marchand *et al.*, Reserves and trade jointly determine exposure to food supply shocks. *Environ. Res. Lett.* **11**, 095009 (2016).

31. A. Robock *et al.*, Climatic consequences of regional nuclear conflicts. *Atmos. Chem. Phys.* **7**, 2003–2012 (2007).

32. FAO, FAOSTAT, United Nation's food and agricultural organization (Rome, Italy, 2019). http://www.fao.org/faostat/. Accessed 10 July 2019.

33. S. Asseng *et al.*, Uncertainty in simulating wheat yields under climate change. *Nat. Clim. Change* **3**, 827–832 (2013).

34. O. Hoegh-Guldberg *et al.*, "Impacts of 1.5 °C of global warming on natural and human systems" in *Global Warming of 1.5 °C. An IPCC Special Report on the Impacts of Global Warming of 1.5°C above Pre-industrial Levels and Related Global Greenhouse Gas Emission Pathways, in the Context of Strengthening the Global Response to the Threat of Climate Change, Sustainable Development, and Efforts to Eradicate Poverty*, V. Masson-Delmotte *et al.*, Eds. (World Meteorological Organization, Geneva, Switzerland, 2018), pp. 175–311. https://www.ipcc.ch/sr15.

35. A. C. Ruane *et al.*, Biophysical and economic implications for agriculture of +1.5° and +2.0°C global warming using AgMIP coordinated global and regional assessments. *Clim. Res.* **76**, 17–39 (2018).

36. K. Hamilton, Early Canadian weather observers and the "year without a summer". *Bull. Am. Meteorol. Soc.* **67**, 524–532 (1986).

37. M. Glotter, J. Elliott, Simulating US agriculture in a modern dust bowl drought. *Nat. Plants* **3**, 16193 (2016).

38. R. L. Naylor, W. P. Falcon, Food security in an era of economic volatility. *Popul. Dev. Rev.* **36**, 693–723 (2010).

39. K. Anderson, S. Nelgen, Agricultural trade distortions during the global financial crisis. *Oxf. Rev. Econ. Pol.* **28**, 235–260 (2012).

40. J. J. Wargent, B. R. Jordan, From ozone depletion to agriculture: Understanding the role of UV radiation in sustainable crop production. *New Phytol.* **197**, 1058–1076 (2013).

41. V. G. Kakani, K. R. Reddy, D. Zhao, K. Sailaja, Field crop responses to ultraviolet-B radiation: A review. *Agric. For. Meteorol.* **120**, 191–218 (2003).

42. L. Xia, J. P. Nowack, S. Tilmes, A. Robock, Impacts of stratospheric sulfate geoengineering on tropospheric ozone. *Atmos. Chem. Phys.* **17**, 11913–11928 (2017).

43. L. M. Mercado *et al.*, Impact of changes in diffuse radiation on the global land carbon sink. *Nature* **458**, 1014–1017 (2009).

44. J. Pongratz, D. B. Lobell, L. Cao, K. Caldeira, Crop yields in a geoengineered climate. *Nat. Clim. Change* **2**, 101–105 (2012).

45. J. Proctor, S. Hsiang, J. Burney, M. Burke, W. Schlenker, Estimating global agricultural effects of geoengineering using volcanic eruptions. *Nature* **560**, 480–483 (2018).

46. D. H. Fleisher *et al.*, A potato model intercomparison across varying climates and productivity levels. *Global Change Biol.* **23**, 1258–1281 (2017).

47. O. B. Toon *et al.*, Atmospheric effects and societal consequences of regional scale nuclear conflicts and acts of individual nuclear terrorism. *Atmos. Chem. Phys.* **7**, 1973–2002 (2007).

48. J. Coupe, C. G. Bardeen, A. Robock, O. B. Toon, Nuclear winter responses to nuclear war between the United States and Russia in the Whole Atmosphere Community Climate Model Version 4 and the Goddard Institute for Space Studies ModelE. *J. Geophys. Res. Atmos.* **124**, 8522–8543 (2019).

49. E. E. Butler, N. D. Mueller, P. Huybers, Peculiarly pleasant weather for US maize. *Proc. Natl. Acad. Sci. U.S.A.* **115**, 11935–11940 (2018).

50. S. Minoli *et al.*, Global response patterns of major rainfed crops to adaptation by maintaining current growing periods and irrigation. *Earth's Future* **7**, 1464–1480 (2019).

51. J. Franke *et al.*, The GGCMI phase II experiment: Global gridded crop model simulations under uniform changes in CO2, temperature, water, and nitrogen levels (protocol version 1.0). *Geosci. Model Dev. Discuss.*, 1–30 (2019).

52. P. J. Crutzen, Albedo enhancement by stratospheric sulfur injections: A contribution to resolve a policy dilemma? *Clim. Change* **77**, 211–219 (2006).

53. A. Robock, Albedo enhancement by stratospheric sulfur injections: More research needed. *Earth's Future* **4**, 644–648 (2016).

54. B. Kravitz, A. Robock, D. T. Shindell, M. A. Miller, Sensitivity of stratospheric geoengineering with black carbon to aerosol size and altitude of injection. *J. Geophys. Res. Atmos.* **117**, D09203 (2012).

55. M. Fromm *et al.*, Pyro-cumulonimbus injection of smoke to the stratosphere: Observations and impact of a super blowup in northwestern Canada on 3-4 August 1998. *J. Geophys. Res. Atmos.* **110**, 1–17 (2005).

56. D. R. Marsh *et al.*, Climate change from 1850 to 2005 simulated in CESM1(WACCM). *J. Clim.* **26**, 7372–7391 (2013).

57. C. G. Bardeen, R. R. Garcia, O. B. Toon, A. J. Conley, On transient climate change at the Cretaceous-Paleogene boundary due to atmospheric soot injections. *Proc. Natl. Acad. Sci. U.S.A.* **114**, E7415–E7424 (2017).

58. G. P. Weedon *et al.*, The WFDEI meteorological forcing data set: WATCH forcing data methodology applied to ERA-interim reanalysis data. *Water Resour. Res.* **50**, 7505–7514 (2014).

59. J. Balkovič *et al.*, Pan-European crop modelling with EPIC: Implementation, up-scaling and regional crop yield validation. *Agric. Syst.* **120**, 61–75 (2013).

60. C. Folberth, T. Gaiser, K. C. Abbaspour, R. Schulin, H. Yang, Regionalization of a large-scale crop growth model for sub-Saharan Africa: Model setup, evaluation, and estimation of maize yields. *Agric. Ecosyst. Environ.* **151**, 21–33 (2012).

61. W. Von Bloh *et al.*, Implementing the nitrogen cycle into the dynamic global vegetation, hydrology, and crop growth model LPJmL (version 5.0). *Geosci. Model Dev.* **11**, 2789–2812 (2018).

62. J. Elliott *et al.*, The parallel system for integrating impact models and sectors (pSIMS). *Environ. Model. Software* **62**, 509–516 (2014).

63. J. W. Jones *et al.*, The DSSAT cropping system model. *Eur. J. Agron.* **18**, 235–265 (2003).

64. W. Liu *et al.*, Global investigation of impacts of PET methods on simulating crop-water relations for maize. *Agric. For. Meteorol.* **221**, 164–175 (2016).

65. W. Mauser *et al.*, Global biomass production potentials exceed expected future demand without the need for cropland expansion. *Nat. Commun.* **6**, 8946 (2015).

66. T. B. Hank, H. Bach, W. Mauser, Using a remote sensing-supported hydro-agroecological model for field-scale simulation of heterogeneous crop growth and yield: Application for wheat in central Europe. *Rem. Sens.* **7**, 3934–3965 (2015).

67. C. Rosenzweig *et al.*, The agricultural model intercomparison and improvement project (AgMIP): Protocols and pilot studies. *Agric. For. Meteorol.* **170**, 166–182 (2013).

68. C. Müller *et al.*, Global gridded crop model evaluation: Benchmarking, skills, deficiencies and implications. *Geosci. Model Dev.* **10**, 1403–1422 (2017).

69. F. T. Portmann, S. Siebert, P. Döll, MIRCA2000 - global monthly irrigated and rainfed crop areas around the year 2000: A new high-resolution data set for agricultural and hydrological modeling. *Global Biogeochem. Cycles* **24**, 1–24 (2010).

70. International Food Policy Research Institute (IFPRI) and International Institute for Applied Systems Analysis (IIASA), Global Spatially-Disaggregated Crop Production Statistics Data for 2005 Version 3.2 (2016). https://doi.org/10.7910/DVN/DHXBJX. Accessed 15 February 2019.

71. D. K. Ray, N. Ramankutty, N. D. Mueller, P. C. West, J. A. Foley, Recent patterns of crop yield growth and stagnation. *Nat. Commun.* **3**, 1293 (2012).

72. C. Folberth *et al.*, Parameterization-induced uncertainties and impacts of crop management harmonization in a global gridded crop model ensemble. *PLoS One* **14**, e0221862 (2019).

73. USDA-PSD, Production, supply and distribution database of the United States department of Agriculture's foreign agricultural service (2019). https://apps.fas.usda.gov/psdonline/app/index.html#/app/home. Accessed 15 February 2019.

74. Natural Earth, Admin 0 countries (2019). https://www.naturalearthdata.com/. Accessed 11 April 2019.